Applied Acoustics 240 (2025) 110949

Contents lists available at ScienceDirect

Applied Acoustics

journal homepage: www.elsevier.com/locate/apacoust

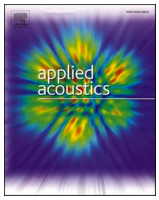

Acoustic muffling of the Sonic Black Holes

Xiaoqi Zhang [a,b], Lilong Wang [a], Li Cheng [d], Heow Pueh Lee [b], Linke Zhang [a,c,*]

[a] School of Naval Architecture, Ocean and Energy Power Engineering, Wuhan University of Technology, Wuhan 430063, PR China
[b] Department of Mechanical Engineering, National University of Singapore, 9 Engineering Drive 1, Singapore 117575, Singapore
[c] Key Laboratory of High Performance Ship Technology, Wuhan University of Technology, Wuhan 430063, PR China
[d] Department of Mechanical Engineering, The Hong Kong Polytechnic University, Kowloon, Hong Kong, PR China

ARTICLE INFO

Keywords:
Sonic black holes
Muffling properties
Muffling mechanism
Multi-peak and broadband muffling

ABSTRACT

Despite the growing interest in Sonic Black Holes (SBHs), existing research predominantly focuses on their sound absorption properties. However, real-life SBH structures, which consist of a finite number of concentric rings, inherently involve both sound absorption and reflection, which differ from the ideal SBHs designed for perfect absorption. Exploration of the muffling characteristics as well as the underlying mechanisms of SBHs are scarce, leaving their properties and underlying principles remain unclear. To bridge this gap, the above issues are investigated numerically and experimentally in this paper, in the context of a linear SBH connected to the main duct as a side branch. Numerical analyses reveal that SBH demonstrates multi-peak, broadband muffling characteristics, and outperforms the muffling performance of traditional quarter-wavelength tube. It was found that when the sound pressure distribution inside the SBH roughly matches odd quarter wavelengths pattern, both the absorption and reflection effects are maximized, resulting in the occurrence of muffling peaks. The SBH induced slow wave effect lowers muffling peak frequencies, creating multiple muffling peaks within the analyzed frequency band. The internal thermal-viscous dissipation effect ensures the broadband muffling performance. The numerically predicted noise attenuation results are validated through comparisons with experimental measurements. While shedding light on the underlying sound attenuation mechanisms, this study leverages the combined effects of partial absorption, reflection, cavity resonances and slow wave phenomena in practical SBHs to develop compact, broadband, low-frequency silencers, providing practical guidelines for future SBH-based muffler designs.

1. Introduction

Duct noise control has attracted considerable attention in the field of acoustics due to its potential negative impacts on the environment and human health [1–5]. While traditional duct noise control methods [6–11] effectively attenuate noise within certain frequency bands, achieving low-frequency and broadband noise reduction remains a major challenge. The rapid advancement of industrialization has significantly increased the demand for effective noise control solutions, calling for innovation and progress in duct noise cancellation technology.

In recent years, acoustic black holes (ABHs) [12] have emerged as an innovative wave control technique. These structures, inspired by the astrophysical concept of black holes, are designed to decelerate wave velocity to zero as waves approach the end of the structure, resulting in effective wave attenuation [12–18]. ABHs are generally classified into Vibrational Black Holes (VBHs) and Sonic Black Holes (SBHs). VBHs are intended for flexural wave manipulation inside vibrating structures, where the structural thickness is tailored according to a power-law relationship. In contrast, SBHs are a variation of ABHs for acoustic wave manipulation in air or fluids. Since the inception of the SBH concept in 2002 [19], substantial efforts have been dedicated to exploring its acoustic properties and practical applications [20–40]. Experimental validations [26–29], including investigations into SBH absorption and reflection performance, have provided crucial insights into SBH behavior. Innovative approaches, such as the transfer matrix method [30,31], fractional-order analysis [25], thermal-viscous analysis [32,33] have further enriched our understanding of SBH characteristics and their potential applications.

Recent studies have expanded the scope of SBH research, exploring acoustic characteristics of open-ended SBH structures [34], enhanced sound absorption in combined SBH structure [35], SBH-conical micro-

* Corresponding author.
E-mail address: lincol@whut.edu.cn (L. Zhang).

https://doi.org/10.1016/j.apacoust.2025.110949
Received 23 January 2025; Received in revised form 12 June 2025; Accepted 13 July 2025
Available online 21 July 2025

perforated panel structure [36,37], folded cavities with SBH [26], and multiple SBHs embedded in waveguides for low-frequency ultra-wideband sound absorption [38]. These endeavors significantly advance our understanding of SBH and pave the way for diverse applications in noise control engineering. It is important to note that most existing studies strive for total sound absorption on idealized SBHs, which differ from real-life implementations. In this paper, we show that the unique physical properties of practical SBHs, including imperfect absorption, partial reflection, resonance and slow sound effects, can be leveraged to design compact, broadband, low-frequency mufflers.

While SBHs demonstrate broadband sound absorption capabilities and substantial progress has been made in understanding their sound absorption mechanisms, research on their muffling properties and underlying mechanisms is fairly limited, with only a few scholars exploring this area. Bravo et al. [39] investigated a pipe muffling structure made up of annular ring resonators with axial gradient of cavity depths. Their simulations and experiments demonstrate effective attenuation and absorption across a wide frequency range, supported by optimized design parameters. Lee et al. [40] proposed a *meta*-silencer containing a coiled multi-slit to generate acoustic black hole effect, and a cavity at the end to further reduce low-frequency noise. Experimental and numerical analyses confirmed that the design provided effective broadband low-frequency noise attenuation. Although, these structures, including annular ring resonators with gradient axial cavity depth and coiled multi-slit configuration, generate acoustic black hole effects, they differ significantly from conventional SBH designs. Research on the muffling characteristics and mechanisms of the traditional SBH structure is still lacking.

To address this gap, the muffling properties and underlying mechanisms of a practical SBH structure with a finite number of concentric rings are scrutinized numerically and experimentally. Unlike some previous studies targeting perfect absorption, our aim is to investigate how the combination of partial absorption, reflection, resonance and slow wave effects in real-life SBH structures can be exploited and leveraged for low-frequency and broadband silencing applications. Specifically, the scenario of an SBH connected to the main duct as a side branch is considered in this paper.

The rest of the paper is organized as follows: the models and equations used for SBH silencing performance assessment and inside sound wave phase velocity distribution derivation are first presented in Section 2. Numerical analyses are then conducted to investigate the muffling properties of SBH alongside the underlying mechanisms in Section 3. Subsequently, the effects of structural parameters on the muffling characteristics of the SBH are fully investigated in Section 4 to provide practical design guidelines. In Section 5, experiments are conducted to validate the established SBH silencing performance assessment FEM model, before major conclusions are summarized.

2. Model

2.1. Conceptual design model

The Sonic Black Hole (SBH) structure investigated in this study, as shown in Fig. 1, comprises a series of rings with varying internal radii, housed within a rigid cylindrical tube. The SBH is characterized by its length L and radius R, with a finite number of embedded rings. The inner radius r of these rings decreases linearly along the axial direction from the inlet to the end of the structure, following the relationship:

$$r(x) = \frac{R}{L}x \tag{1}$$

where x represents the longitudinal position along the SBH axis. In this study, the SBH is designed with the following parameters: $R = 30$ mm, $L = 200$ mm, and a ring thickness of 2 mm. The last ring is positioned 20 mm from the end, while the remaining rings are spaced 18 mm apart, giving a total of nine rings.

2.2. Muffling performance analysis model

As illustrated in Fig. 2a, the scenario in which the SBH is flush-mounted on the duct wall as a side branch is considered for the investigation of its silencing performance. To ensure an accurate evaluation,

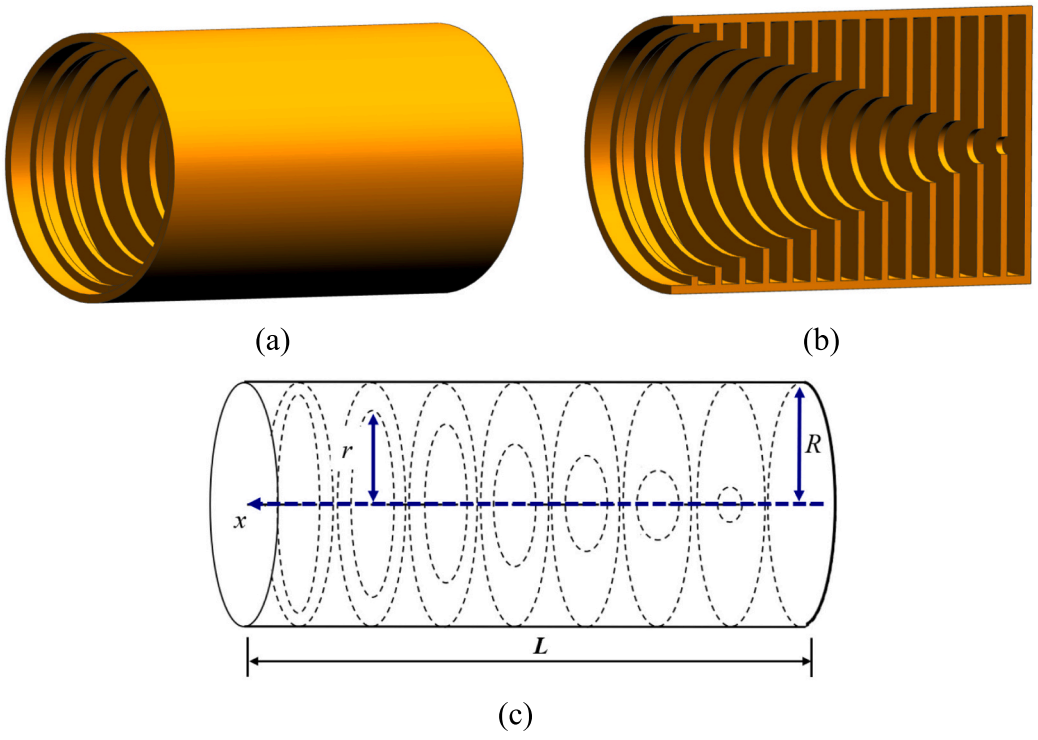

Fig. 1. Investigated SBH structure: (a) overall view; (b) detailed internal configuration; (c) schematic diagram.

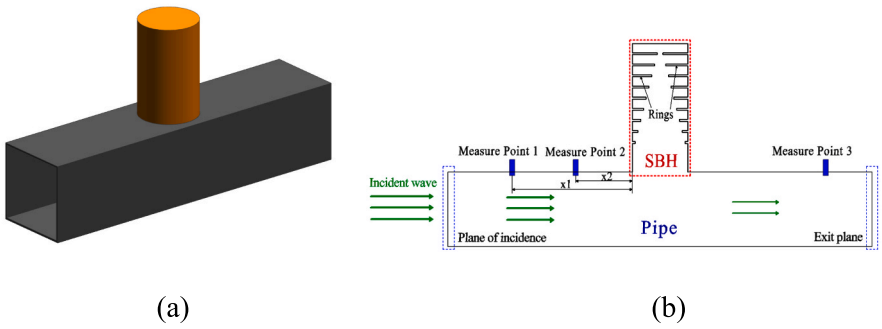

Fig. 2. Schematic of (a) SBH flush-mounted on the duct wall as a side branch; (b) SBH acoustic characteristics calculation model.

the Thermo-Viscous Acoustics interface in commercial software COMSOL Multiphysics was employed. This approach accounts for the thermo-viscous dissipation within the SBH by solving the Linearized Navier-Stokes (LNS) equations.

The schematic diagram of SBH acoustic characteristics calculation model is shown in Fig. 2b. A plane wave with an amplitude of 1 Pa was applied at the duct inlet, while a plane wave radiation boundary condition was applied at the duct end. This ensures that the end of the duct can be treated as an ideal boundary, eliminating reflections.

Two acoustic pressure monitor points are positioned upstream the sample. The sound pressure at point 1 and point 2, donated as p_1 and p_2, can be written as:

$$p_1 = P_I e^{ik_0 z_1} + P_R e^{-ik_0 z_1} \tag{2}$$

$$p_2 = P_I e^{ik_0 z_2} + P_R e^{-ik_0 z_2} \tag{3}$$

where z_1 and z_2 are the distances from the sample to points 1 and 2, respectively; P_I and P_R are the amplitudes of the incident wave and reflected wave in the duct; i is the imaginary unit; $k_0 = \omega/c = 2\pi f/c$ is the wave number; c is the sound speed; ω is the angular frequency of the acoustic wave; f is the acoustic wave frequency.

By solving Eqs. (2) and (3), the sound energy reflection coefficient r can be determined as follows:

$$r = \frac{P_R^2}{P_I^2} \tag{4}$$

The energy transmission coefficient τ and the sound absorption coefficient α are given as:

$$\tau = \frac{P_T^2}{P_I^2} \tag{5}$$

$$\alpha = 1 - |r| - |\tau| \tag{6}$$

where P_T represents the transmitted sound pressure, which corresponds to the sound pressure at point 3.

Transmission loss (TL) of SBH can be determined as:

$$TL = 10\lg\frac{1}{\tau} \tag{7}$$

The analyzed frequency range is constrained by the plane wave assumption. The maximum frequency for analysis should below the cutoff frequency of the rectangular duct, which is determined through equation (8) below.

$$f_c = \frac{c}{2L_x} \tag{8}$$

where L_x denotes the side length of the square duct. In this study, $Lx =$ 100 mm, $f_c = 1715$ Hz.

Thermo-viscous dissipation primarily occurs within the viscous boundary layer, making proper meshing of this region essential for thermal-viscous acoustic simulations. Conventionally, the boundary layer thickness, δ, determined through Eq. (9), guides the design of the mesh dimensions in the acoustic boundary layer:

$$\delta = \sqrt{\frac{2\mu}{\rho_0 \omega}} \tag{9}$$

where μ is the dynamic viscosity.

The thickness of the boundary layer is frequency-dependent, decreasing as the frequency increases. At a maximum incident frequency of 1600 Hz under standard atmospheric conditions (20°C, 1 atm), with air density $\rho_0 = 1.21$ kg/m^3 and dynamic viscosity $\mu = 1.8 \times$ 10–5 Pa-s, the boundary layer thickness at this highest frequency is approximately 0.055 mm. Additionally, the slowing acoustic wave velocity toward the SBH end leads to a further reduction in the boundary layer thickness. Based on our previous research [33] this reduced thickness is approximated as one-sixth of its normal value. To ensure precision, a five-layer grid with an expansion coefficient of 1.2 is applied to the boundary layer region, with the minimum layer thickness of 0.0012 mm. Beyond the acoustic boundary layer region, a guideline of at least six cells per wavelength is followed to discretize the computational domain, ensuring accurate resolution of acoustic wave fluctuations. To ensure truthful representation of the geometrical details inside the SBH, a minimum mesh size of approximately 1/60 of the maximum element size, around 0.55 mm, is adopted. Given that the smallest internal diameter of the SBH inside rings is about 6 mm and the thickness of the rings is 2 mm, the selected minimum mesh size guarantees sufficient resolution of the SBH internal features. This refined meshing strategy enables high-fidelity acoustic analysis, capturing the critical thermo-viscous effects essential for evaluating silencing performance of SBH. The discretized computational domain is shown in Fig. 3.

The convergence of the solution in relation to the meshing is conducted and the results indicate that convergence can be achieved by using 200,000 elements to ensure the accuracy needed for transmission loss prediction.

2.3. Phase velocity derivation model

2.3.1. WKB model

As shown in Fig. 4, the SBH under investigation here can be considered as a series of cavities tightly interconnected in sequence. The dashed line in Fig. 4b forms the waveguide with varying cross section and wall admittance along the wave propagation direction. In such, considering x-axis as the symmetry axis of the waveguide and a thin air layer of thickness dx, the law of conservation of mass gives:

$$d(\rho_0 Sv) + (2\pi r v_+ \rho_0)dx + \frac{\partial \rho}{\partial t} S dx = 0 \tag{10}$$

where v is the sound particle velocity; S is the cross-sectional area of the thin layer, r is the inner radius; and v_+ is the projection of the particle

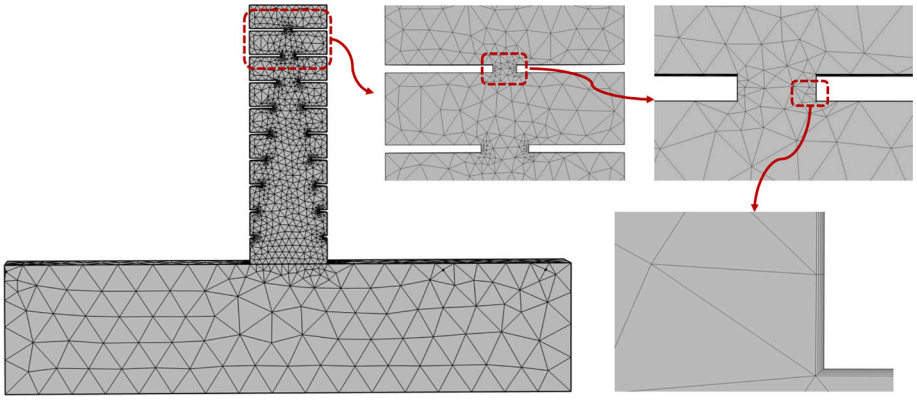

Fig. 3. Sketch of the discretized computational domain.

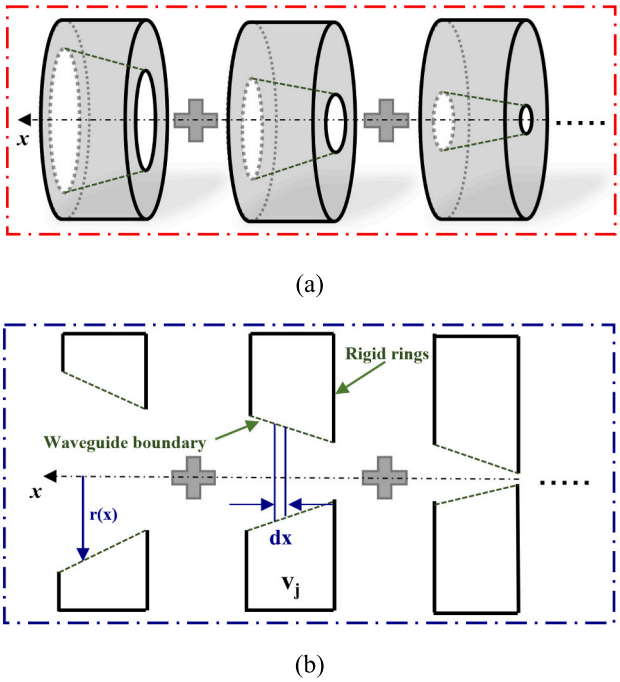

Fig. 4. SBH inside cavities: (a) 3-dimensional view; (b) 2-dimensional view.

velocity at wall admittance along the direction perpendicular to the axis of symmetry.

The relationship between the velocity v_+ and the pressure p is:

$$v_+ = Y_j p \tag{11}$$

where Y_j denotes the admittance of the waveguide wall in cavity j.

According to Newton's second law and equation of state, we have

$$-\frac{\partial p}{\partial x} = \rho_0 \frac{\partial v}{\partial t} \tag{12}$$

$$\frac{\partial \rho}{\partial t} = \frac{1}{c^2}\frac{\partial p}{\partial t} \tag{13}$$

For pressure varying harmonically in time, after combining the above four equations we obtain:

$$p'' + p'(\ln S)' + p\left(k_0^2 + \frac{2Y_j\rho}{r}(i\omega)\right) = 0 \tag{14}$$

where k_0 is the wave number in the air.

For a realizable SBH structure composed of a limited number of discrete concentric rings, the finite spacing between the rings leads to discontinuities in the surface admittance of the waveguide formed in SBH, and thus, a discretized impedance boundary treatment should be adopted. This differs from the idealized SBH model studied in reference [19], where a large number of closely spaced rings allow for continuous description of the surface admittance. This results in a different form of wave number expression and sound velocity compared to that in [19]. In our case, the impedance of the wall of the waveguide in cavity j can be written as [41]:

$$Z_{total-j} = \frac{Z_0 S_j}{k_0 V_j} i = B_j i \tag{15}$$

where Z_0 is the characteristic impedance of the air; S_j is the area of the surface impedance boundary in cell j and V_j is the volume of the backing cavity.

$$(\ln S)' = \frac{1}{S}S' = \frac{2\pi r r'}{\pi r^2} = \frac{2r'}{r} = 2(\ln r)' \tag{16}$$

$$Y_j = \frac{1}{Z_{total-j}} \tag{17}$$

After taking into account of the above relations (Eqs. (16) and (17)), Eq. (14) is simplified as follows,

$$p'' + 2p'(\ln r)' + p\left(k_0^2 + \frac{2\rho_0\omega}{rB_j}\right) = 0 \tag{18}$$

The Wentzel-Kramers-Brillouin (WKB) approximation is used to solve Eq. (18). We assume that $p(x) \sim \exp(ikx)$ and substitute this expression into Eq. (18). Then, Eq. (18) can then be rewritten in terms of the local wave number k as follows:

$$-k^2 + 2ik(\ln r)' + \left(k_0^2 + \frac{2\rho_0\omega}{rB_j}\right) = 0 \tag{19}$$

Solving Eq. (19) yields the local wave number k_j (x) in cell j as:

$$k_j(x) = \sqrt{k_0^2 + \frac{2\rho_0\omega L}{Rx\frac{Z_0 S_j}{k_0 V_j}} - \frac{1}{x^2}} \tag{20}$$

The corresponding phase and group velocities can be obtained as:

$$c_p = \frac{\omega}{k} = \frac{2\pi f}{\sqrt{k_0^2 + \frac{2k_0 V_j \rho_0 \omega L}{Z_0 S_j R x} - \frac{1}{x^2}}} \tag{21}$$

$$c_g = \frac{d\omega}{dk} = \left(\frac{dk}{d\omega}\right)^{-1} \tag{22}$$

Equations (20) – (22) are critical in determining the spatial variation

of wave velocity and provide insights into the phase velocity, group velocity, and phase velocity distribution of sound wave inside the SBH structure. In particular, the reduction in phase velocity illustrates the slow wave effect induced by the SBH, which plays a vital role in generating muffling peaks on TL curves. Equations (20) – (22) relate the resulting phase delay to the formation of muffling peaks and quantitively explain the appearance of peak frequencies in TL spectra, the underlying mechanism of SBH-induced broadband and low-frequency sound attenuation and support the physical interpretation of the simulation and experimental results presented in later sections.

It should be noted that the WKB approximation is valid when the coefficient in Eq. (18) shows only slight variations within the wavelength range. Consequently, this leads to the following two inequalities [41]:

$$C_1 = |k| - \left|\frac{1}{x}\right| > 0 \tag{23}$$

$$C_2 = |k| - \left|\frac{2L^2}{x(L^2 - x^2)}\right| > 0 \tag{24}$$

2.3.2. Time-domain FEM model

To investigate the acoustic wave propagation behavior inside the SBH, time-domain FEM analysis is conducted. The model is shown in Fig. 5, in which Pressure Acoustics Transient Physics is applied throughout the entire model. A sinusoidal wave with one period at a given frequency is incident into the duct from the left-hand side. A Perfectly Matched Layer (PML) is applied at the end of the main duct to ensure a reflection-free boundary condition. Point probes are positioned along the center axis of the SBH at intervals of $L = 20\ mm$ to calculate the phase velocity of the acoustic wave based on the displacement–time relationship. The meshing process follows the method described in Section 2.2.

3. Results and analyses

3.1. Muffling performance analysis

The calculated TL curve of SBH within the frequency range of 100–1600 Hz is presented in Fig. 6. A cavity structure, modeled as a traditional quarter-wavelength tube with identical length and radius to the SBH, was also analyzed using identical arrangement and methods. The TL curves of both structures are compared and presented in Fig. 6.

As shown in Fig. 6, the SBH structure exhibits five distinct muffling peaks within the analyzed frequency range. These peaks occur at 280 Hz, 550 Hz, 870 Hz, 1220 Hz, and 1570 Hz, with each peak amplitude exceeding 5 dB. The highest peak observed at 870 Hz, reaches 9.4 dB. Between these peaks, the SBH structure demonstrates broadband muffling, with an average muffling level of 1.6 dB. Overall, the SBH structure exhibits broadband and multi-peak muffling characteristics.

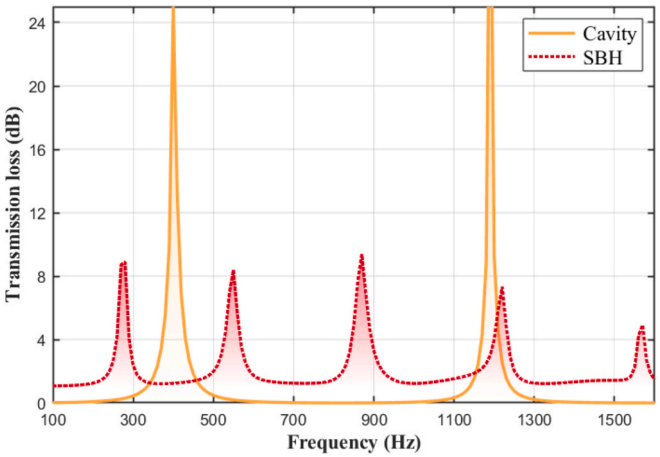

Fig. 6. Comparison of TL curves between SBH and cavity structure.

In contrast, the TL curve of the cavity structure shows muffling peaks only at 400 Hz and 1190 Hz within the analyzed frequency range. At non-peak frequencies, the muffling level is nearly zero, indicating highly frequency-specific and narrowband muffling behavior.

Quantitatively, the mean muffling capacity of the SBH is 2.13 dB per frequency, while that of the cavity is 1.01 dB. The muffling capacity of the SBH muffler is 2.12 times greater than that of a traditional quarter-wavelength tube, demonstrating superior sound attenuation performance.

3.2. Muffling mechanism analysis

Fig. 7 shows the sound absorption and reflection coefficients for the SBH and the cavity structures. The results reveal that the SBH exhibits high sound absorption and reflection coefficients at peak muffling frequencies, with both effects contributing to its overall muffling performance. Even at non-peak frequencies, the SBH maintains certain sound absorption, which underpins its broadband muffling characteristics. In contrast, conventional cavity structure relies solely on sound wave reflection for muffling, completely lacking sound absorption capabilities. As a result, the cavity achieves muffling effects only at specific frequencies, exhibiting narrowband muffling behavior.

We define the total power dissipation density as Δ (SI unit: W/m^3), which represents the energy dissipated per unit volume through both viscous and thermal effects, as described in [42–45]:

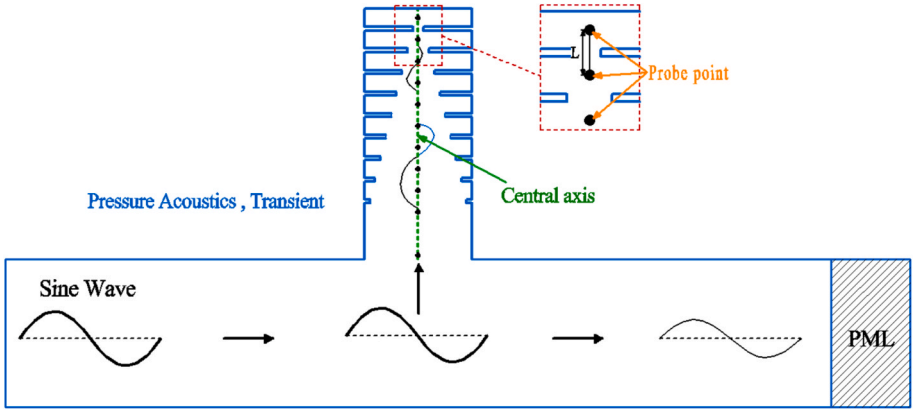

Fig. 5. Schematic diagram of time-domain FEM analysis model.

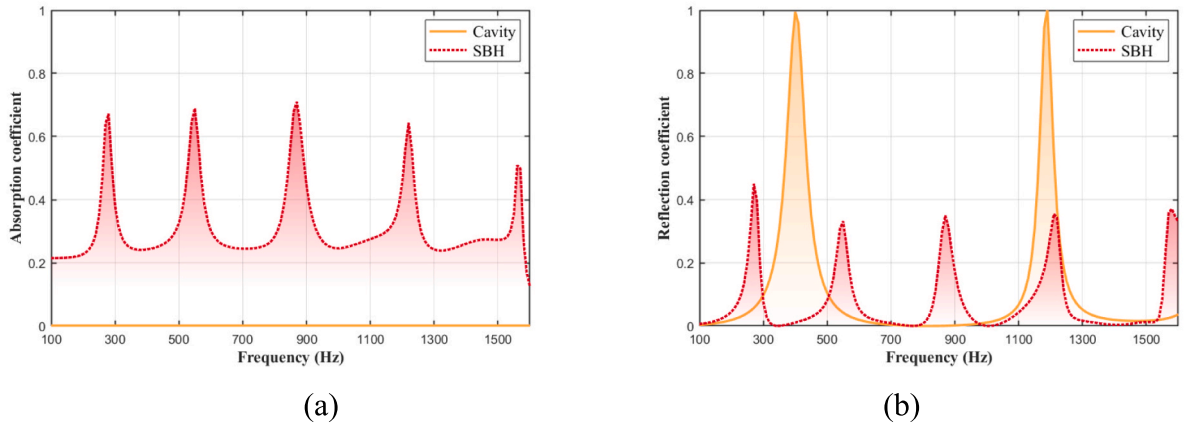

Fig. 7. Comparison of acoustic properties between SBH and cavity: (a) absorption coefficient; (b) reflection coefficient.

$$\Delta = \Delta_v + \Delta_t = \tau : \nabla u_1 + \frac{\kappa}{T_0}(\nabla T_1)^2 \tag{25}$$

where $\boldsymbol{\tau}$:∇ $\boldsymbol{u_1}$ is the viscous dissipation function; ":" denotes the double dot operator (or total inner product); $\boldsymbol{\tau}$ is the viscous stress tensor; Δ_v and Δ_t are the viscous and thermal contributions to the dissipation function, respectively.

The total power dissipation density, Δ, calculated at different peak frequencies using Eq. (25), is presented in Fig. 8 to quantify the thermo-viscous dissipation in SBH. The results reveal that, upon entering the SBH, the sound wave experiences substantial thermo-viscous dissipation. This dissipation, primarily due to viscous effects, converts a portion of the acoustic energy into thermal energy, enhancing the sound absorption performance and significantly contributing to the broadband muffling effect.

To further explore the multi-peak muffling behavior of the SBH, the sound pressure distributions along the center axis of the SBH and the cavity structures at their peak frequencies are presented in Figs. 9 and 10. The short orange lines are approximate in length, which is manually placed at pressure extrema and zero-crossings. They serve as a visual tool to facilitate counting quarter-wavelength segments; their irregular spacing reflects the position-dependent wave speed variation. Precise calculation based on local wavenumber was not performed to determine the exact position of these markers. Fig. 10 shows that at cavity muffling peak frequencies of 400 Hz and 1190 Hz, the sound pressure distribution along the center axis of the cavity corresponds to 1/4 and 3/4 wavelengths of the incident wave. According to reference [46], when odd multiples of 1/4 wavelength of incident wave enter the cavity, the reflected wave returns to the main duct and superimposes with the incident wave of opposite phase, resulting in totally cancellation and a peak muffling effect. Fig. 9 shows that the acoustic wave propagating inside the device undergoes compression, with its wavelength gradually shortening as it approaches the SBH end, and the wave pattern is distorted and significantly different from that in the straight duct section. After compression, the sound pressure distributions inside SBH correspond to 1/4, 3/4, 5/4, 7/4, and 9/4 wavelength patterns at five TL peak frequencies. The wave patterns in SBH at peak muffling frequencies are consistent with those of cavity structure observed at its TL peaks, indicating that the muffling mechanism due to reflection at TL peaks is identical for the SBH and the cavity structure. However, the TL peaks of the SBH are significantly shifted to lower frequencies compared to cavity structures, and the intervals between adjacent TL peaks are notably

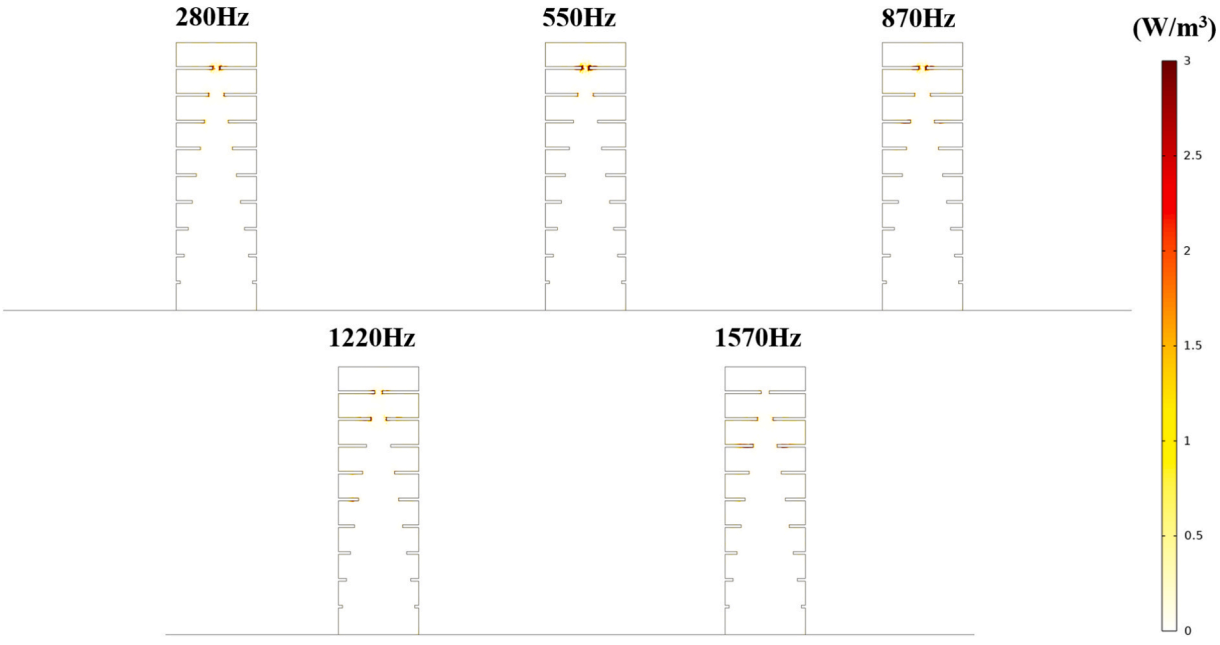

Fig. 8. Power density inside the SBH at different peak muffling frequencies.

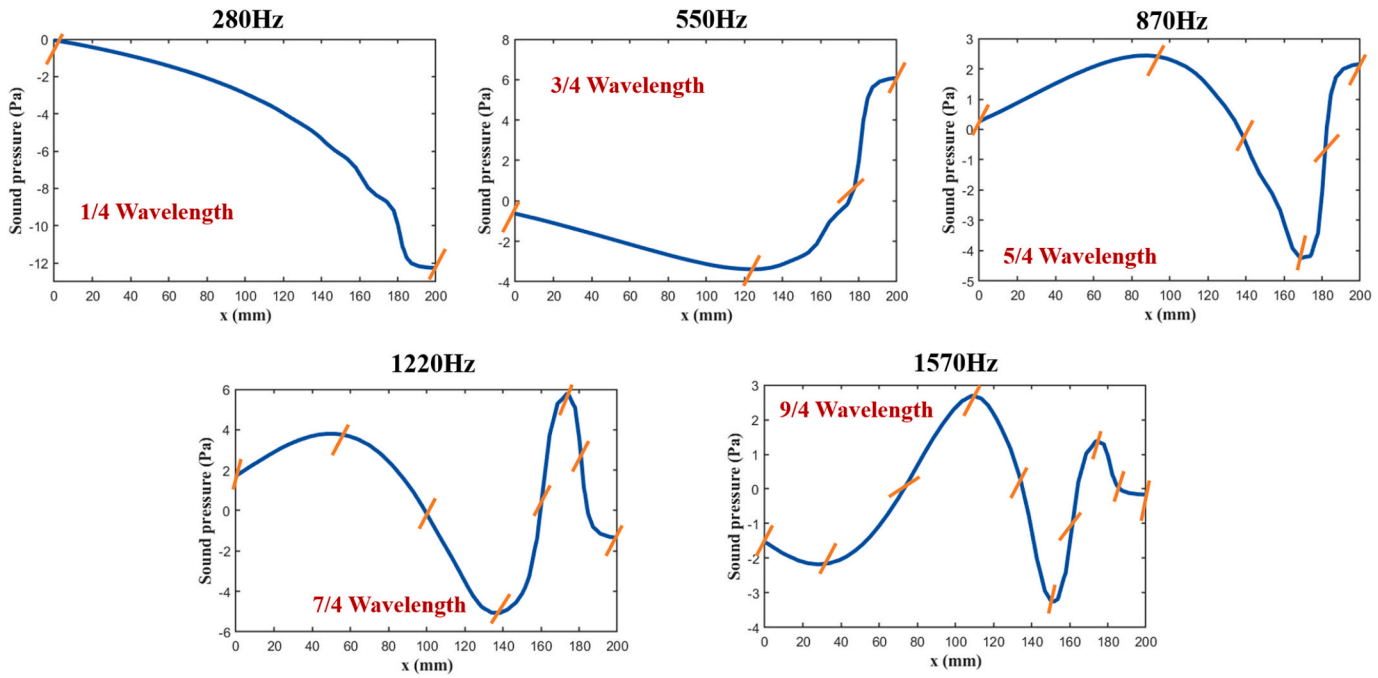

Fig. 9. Sound pressure distributions along the center axis of the SBH at different peak frequencies. The short orange lines discretize and segment the sound pressure waveform into 1/4 wavelength regions, with each pair of lines corresponding to a 1/4 wavelength.

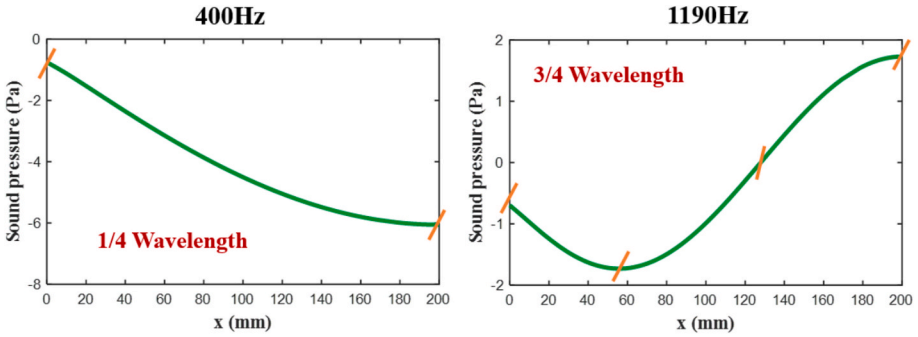

Fig. 10. Sound pressure distributions along the center axis of the cavity at different peak frequencies. The short orange lines discretize and segment the sound pressure waveform into 1/4 wavelength regions, with each pair of lines corresponding to a 1/4 wavelength.

smaller, resulting in a greater number of TL peaks appear within the analyzed frequency range.

To gain further insight into the underlying causes of the observed downshifting of SBH TL peaks, time-domain FEM analysis, as detailed in Sec. 2.3, was conducted. This approach enables the observation of transient wave phenomena, such as local phase delay and slow sound effects, which are difficult to capture using frequency-domain methods. The CFL (Courant–Friedrichs–Lewy) condition was strictly satisfied in the simulations. The time step was set to 0.01 ms, and a minimum mesh size of approximately 1/60 of the maximum element size, namely around 0.55 mm, was adopted. This results in a CFL number of approximately 6. However, it should be noted that as the sound wave propagates into the SBH structure, its velocity decreases gradually, causing a further reduction in the CFL number. Dense meshes with minimum size are located near the end of the SBH, where the wave velocity decreases to less than 1/5 of its initial value. Consequently, the CFL number further reduces to near 1 in the critical regions, which is sufficiently small to ensure numerical stability in transient simulations. Fig. 11 depicts the sound pressure distribution curves inside the SBH at different monitor points in time, corresponding to different TL peak frequencies. The results illustrate that over time, the sinusoidal wave undergoes morphological changes, including variations in both amplitude and period. The peak of the sound wave shifts slightly forward in time, while the valley moves significantly farther, resulting in a gradual reduction in the peak-to-valley distance. This observation indicates that the wavelength of the sound wave is compressed, leading to a reduction in the wave velocity, which is proportional to the wavelength, as it propagates through the SBH.

In previous studies, such as Umnova et al. [47], the sound wave phase velocity distribution inside SBH structures was analyzed primarily to qualitatively explain the observed shift in the peak frequencies of sound absorption for different SBH profiles. In this work, we intend to quantitatively investigate the influence of internal wave velocity distribution on the formation of TL peaks. To this end, the phase velocity distribution of sound wave within the SBH is first calculated using both the FEM and WKB models, as described in detail in Section 2.3. According to Eqs. (23) and (24), the WKB approximation is valid when the frequency exceeds 500 Hz. Consequently, this paper starts the calculation from the frequency of the second TL peak, which is 550 Hz. The reliability of the results is ensured by comparing the WKB-derived phase velocity profile against time-domain FEM simulations across the frequency range of interest. The comparison of results, presented in Fig. 12,

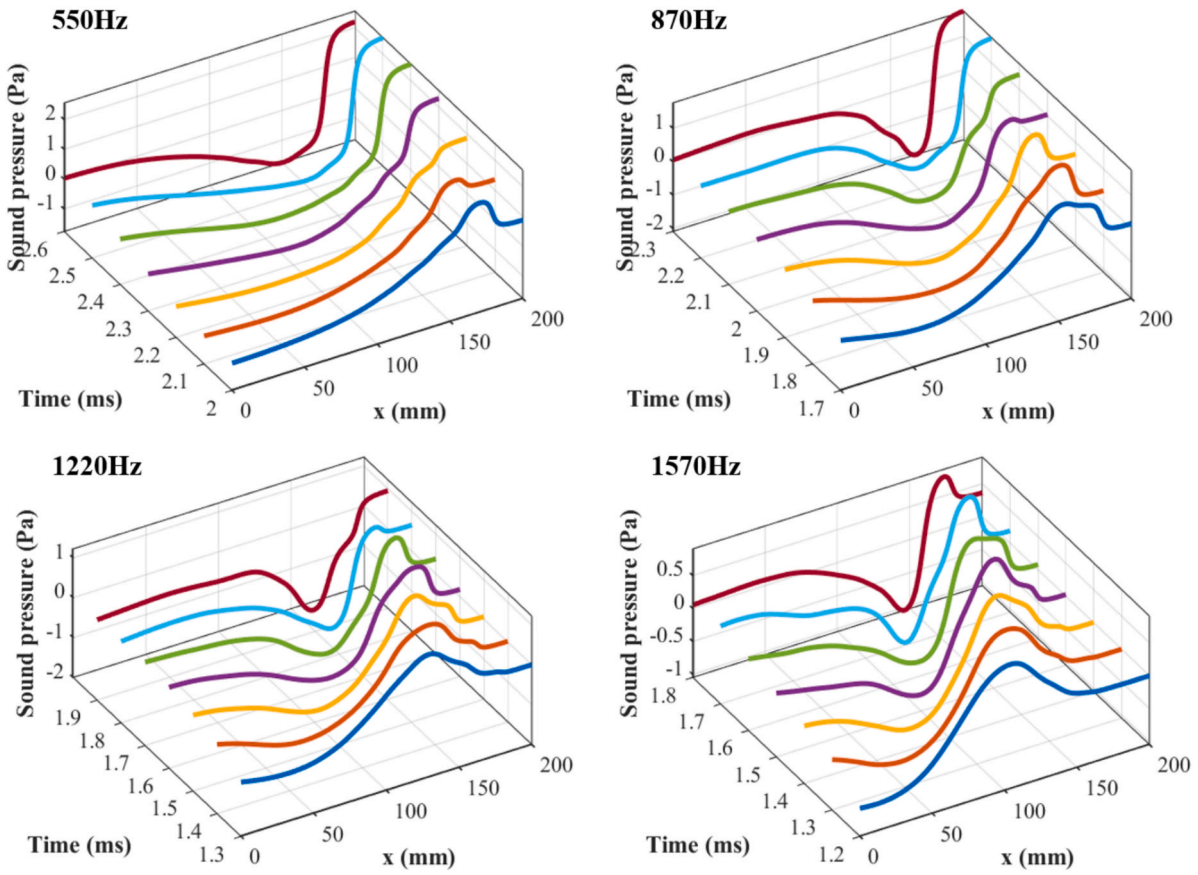

Fig. 11. Sound pressure distribution curves inside the SBH at various monitor points over time at different TL peak frequencies.

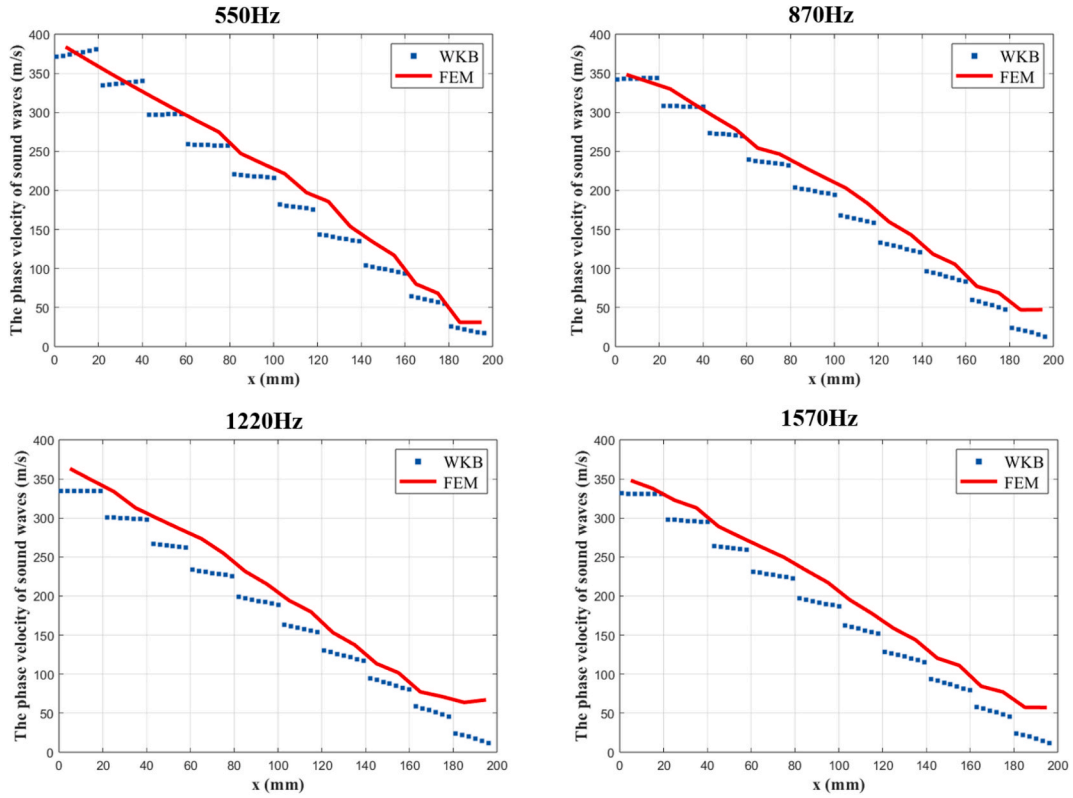

Fig. 12. Variation in the phase velocity inside the SBH at different frequencies.

reveals a minor difference between the sound velocities calculated by the two models, except for a notable discrepancy observed near the end of the structure. This discrepancy arises from the interference of reflected waves at the end of the structure in the FEM method. In the remaining sections, the velocities calculated by both models align closely.

The WKB method reveals that the phase velocity within each cavity of the SBH is approximately linearly distributed, while the overall phase velocity distribution across the SBH is non-linear. Based on this observation, the mean phase velocity of sound wave $\overline{c_j}$ for the j-th cavity is calculated by averaging the phase velocities at its two ends. Furthermore, to effectively characterize the overall propagation behavior and identify the locations of the TL peaks, the harmonic mean [48], which is defined as the reciprocal of the arithmetic mean of the reciprocals of individual measurements, is introduced to account for the non-linear spatial variation of wave velocity and determine the overall mean phase velocity in the SBH. It is especially useful for calculating the average velocity in sections with varying speeds and enables the quantitative prediction of TL peaking frequencies, thereby providing a more comprehensive understanding of the sound attenuation mechanisms in SBHs. The time $t_j = l_j/\overline{c_j}$ for the sound wave to pass through the j-th cavity of SBH with length l_j is first determined. The total time for the sound wave to traverse the entire SBH is then obtained by summing t_j over all cavities. The overall mean phase velocity of sound wave within the SBH is calculated by dividing the total length of the SBH by the total passage time. This process is mathematically expressed as:

$$\overline{c_h} = \frac{ml_j}{\sum_{j=1}^{m} \frac{l_j}{\overline{c_j}}} = \frac{m}{\sum_{j=1}^{m} \frac{1}{\overline{c_j}}} \tag{26}$$

where m denotes the number of cavities in SBH.

The SBH achieves muffling peaks when the internal wave patterns correspond to odd multiples of one-quarter wavelength, expressed as:

$$\frac{n}{4}\lambda = L(n = 1, 3, 5, 7, 9\cdots\cdots) \tag{27}$$

Based on the relationship between frequency, the overall mean phase velocity and wavelength, the frequency of SBH muffling peak is determined as:

$$f = \frac{\overline{c_h}}{\lambda} = \frac{mn}{4L}\left(\sum_{j=1}^{m} \frac{1}{\overline{c_j}}\right)^{-1} \tag{28}$$

Table 1 presents a comparison of the muffling peak frequencies calculated using Eq. (28) with those derived from the TL curves in Fig. 6, calculated from FEM model. The results indicate that the muffling peak frequencies predicted by the Average Waves Velocity method through Eq. (28) are in close agreement with those obtained from FEM model, with a maximum relative difference $\Delta = |f_{FEM} - f_{ASS}|/|f_{FEM}|$ below 15 %. This confirms the accuracy and reliability of the Average Wave Velocity method for predicting SBH muffling peak frequencies. The differences primarily arise from the complexity of wave propagation at the SBH end. The above analysis provides a qualitative explanation of the relationship between phase velocity of and the location of TL peak frequency. The overall mean phase velocity of sound wave in the SBH at five TL peak frequencies calculated through Eq. (26) are 194.5 m/s, 128.5 m/s, 143.8 m/s, 147.4 m/s and 142.3 m/s, all lower than the nominal wave velocity, suggesting that the down-shifting of the SBH muffling peak frequency is primarily associated with the reduction in sound wave velocity.

Table 1
Comparison of TL peak frequencies calculated by Eq. (28) and FEM model.

f (Hz)	Peak 1	Peak 2	Peak 3	Peak 4	Peak 5
FEM model	280	550	870	1220	1570
Average Wave Velocity method	243	480	899	1289	1675

In summary, the SBH exhibits both broadband and multi-peak muffling characteristics. The broadband muffling arises primarily from thermo-viscous dissipation within the SBH, enabling sound absorption and ensuring an effective broadband muffling effect. The SBH achieves muffling peaks when the internal sound pressure distribution pattern corresponds to odd multiples of 1/4 wavelengths. This multi-peak muffling behaviour is ascribed to SBH-induced slow wave effect, which compresses the waves entering into SBH, effectively increases the SBH length and lowers the frequency of the muffling peaks, thereby enabling the structure to exhibit multi-peak muffling within a specified frequency band.

4. Effects of structural parameters

4.1. Effect of ring number

To provide guidance for the SBH muffling performance optimization, the effects of its structural parameters are scrutinized. The influence of the number of inside embedded rings is examined first. The TL curves of SBHs with 6, 9, 14, and 19 rings, while maintaining the total length, ring thickness, and cavity radius constant, are computed and presented in Fig. 13.

Fig. 13 illustrates that the 6-ring SBH exhibits four TL peaks, whereas the 19-ring SBH displays six TL peaks and the mean muffling effects within the analyzed frequency range for the SBH structures with 6, 9, 14, and 19 rings were 2.31 dB, 2.13 dB, 2.24 dB, and 2.32 dB, respectively. As the number of rings increases, the TL peaks are down-shifted to lower frequencies, the number of muffling peaks increases, and the bandwidth of these peaks widens. However, the amplitudes of these TL peaks decrease. In general, the total muffling performances for SBHs with different numbers of rings remain relatively consistent. To better understand the downshifting of TL peaks, as an example, the phase velocity distributions inside SBHs with different number of rings at their fourth TL peak frequency were calculated. The results, shown in Fig. 14, along with the calculated overall mean wave velocity listed in Table 2, indicate that as the number of rings increases, the wave velocity within the SBH decreases. Consequently, the TL peak frequencies decrease, leading to a downward shift in the TL peaks as the number of rings increases. It should be noted that Eq. (22) describes phase velocity distribution for a practical SBH structure with a finite number of rings, in which the surface impedance of the inner waveguide wall is treated as discontinuous due to the discrete ring arrangement. As the number of rings increases and the distance between adjacent rings decreases, the discrete SBH structure gradually approaches the ideal continuous SBH case. In this situation, the impedance distribution and the internal waves velocity profile tend to be continuous. This explains why, as observed in

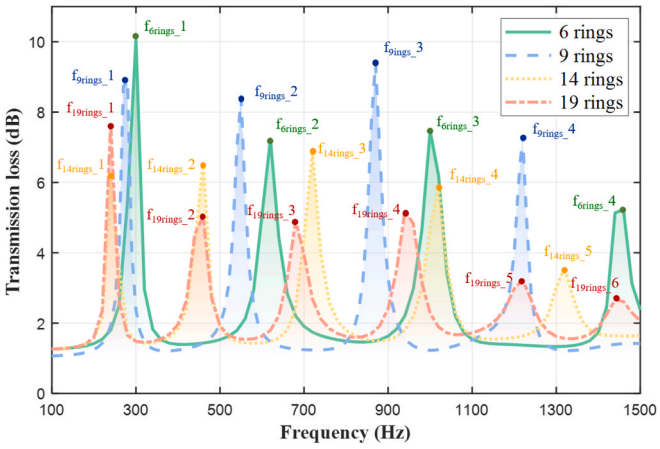

Fig. 13. TL curves for SBH with different number of rings.

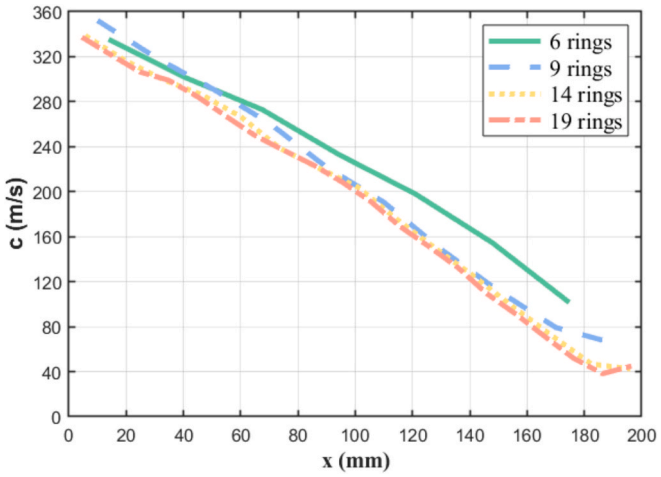

Fig. 14. Phase velocity distribution inside SBHs with different numbers of rings at the fourth TL peak.

Table 2
Overall mean phase velocity of SBHs with varying number of rings at the fourth TL peak.

	6 rings	9 rings	14 rings	19 rings
$f_{\_4}$ (Hz)	1440	1220	1020	940
$\overline{c_h}$(m/s)	196.8	147.4	127.2	120.1

Figs. 13 and 14, the resonance frequency shift when the number of rings increases from 14 to 19 becomes less significant, as compared with cases with a smaller number of rings, indicating that quasi-continuous state has already sufficiently approached using 14 or more rings. While increasing the number of rings inside the SBH has little effect on the total muffling performance, assuming the total length and radius remain unchanged, it enhances the waves velocity modulation ability of the SBH, resulting in a greater number of muffling peaks within a specific frequency range.

4.2. Effect of SBH radius

The effect of the radius (R) on the silencing performance of the SBH is subsequently examined. The radius is varied among 20 mm, 30 mm, 40 mm, and 50 mm, while keeping the other structure parameters constant. Additionally, the inner radius of the rings was adjusted according to the relationship specified in Eq. (1). The calculated TL curves for each configuration are shown in Fig. 15. The mean acoustic attenuations for

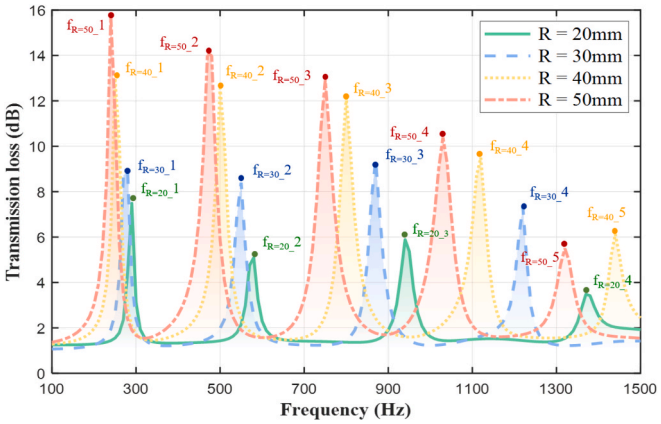

Fig. 15. TL curves for SBHs with different radii.

SBHs with different radii are quantified as 1.85 dB, 2.13 dB, 3.04 dB and 3.48 dB. These results indicate that increasing the radius significantly improves the overall muffling performance of the structure, probably due to the increased contact area between the SBH and the duct, which enhances its interaction with the sound wave. These results indicate that increasing the radius significantly improves the overall muffling performance of the structure, probably due to the increased contact area between the SBH and the duct, which enhances its interaction with the sound wave.

To gain deeper insights, the proportions of absorbed, reflected, and transmitted acoustic energy during the propagation of acoustic waves through the SBH with different radii are calculated and presented in Fig. 16. The results show that the energy absorbed by the SBH slightly increases as the radius grows. However, the reflected energy exhibits a substantial rise, increasing from 4 % at $R = 20$ mm to 16 % at $R = 50$ mm, which indicates a marked improvement in reflection. Consequently, increasing the radius of the SBH effectively improves its sound reflection capability, thereby enhancing its overall silencing performance.

4.3. Effect of SBH length

To examine the impact of structure length on the muffling performance, the SBH length is varied among 100 mm, 200 mm, 300 mm and 400 mm, while keeping the number of rings and SBH radius constant. The inner radius of the rings is adjusted according to the relationship specified in Eq. (1). The TL curves corresponding to SBHs with different lengths were calculated and presented in Fig. 17.

The results indicate that as the length increases, the magnitudes of TL peaks rise, while the attenuation bandwidth near TL peak becomes narrower, making the peaks sharper and less smooth. The TL peaks shift to lower frequencies, and the frequency intervals between neighboring peaks decrease, as quantified in Fig. 18. As a result, more TL peaks emerge within the analyzed frequency range. Although the number and values of TL peaks increase, the narrower bandwidths around the peak frequencies makes increasing the SBH length has little effect on its overall acoustic attenuation performance. Within the studied frequency range, the mean noise reduction for the SBH structures with lengths of 100 mm, 200 mm, 300 mm, and 400 mm were 2.20 dB, 2.13 dB, 2.30 dB, and 2.31 dB, respectively. As analyzed in Sec.3.2, the muffling peak occurs when the sound pressure distribution inside SBH corresponds to odd multiples of one-quarter wavelength. As the structure length increases, although the inside overall mean waves velocity increases, for instance, at 1000 Hz, as listed in Table 3, the inside sound pressure distribution corresponds to waves of a greater wavelength in longer SBHs. This ultimately results in a down-shifting of peak frequencies and the emergence of additional muffling peaks within the analyzed frequency band.

In light of the aforementioned analysis, we conclude guidelines for designing an effective silencing device by tuning the SBH structural parameters. Our findings suggest that enhancing the muffling peak performance of the SBH is contingent upon an appropriate augmentation of its structure length and radius. While increasing the structural size of SBH and the number of internal rings can broaden the muffling bandwidth and improve the low-frequency muffling performance, when the available installation space is constrained, enhancing the number of embedded rings to improve its silencing performance is preferable to keep SBH compact.

5. Experimental validations

5.1. Prototype and Test-rig

Experiments were conducted to validate the SBH silencing performance prediction model. The test sample, depicted in Fig. 19, was meticulously designed and fabricated using aluminum alloy. A cylinder

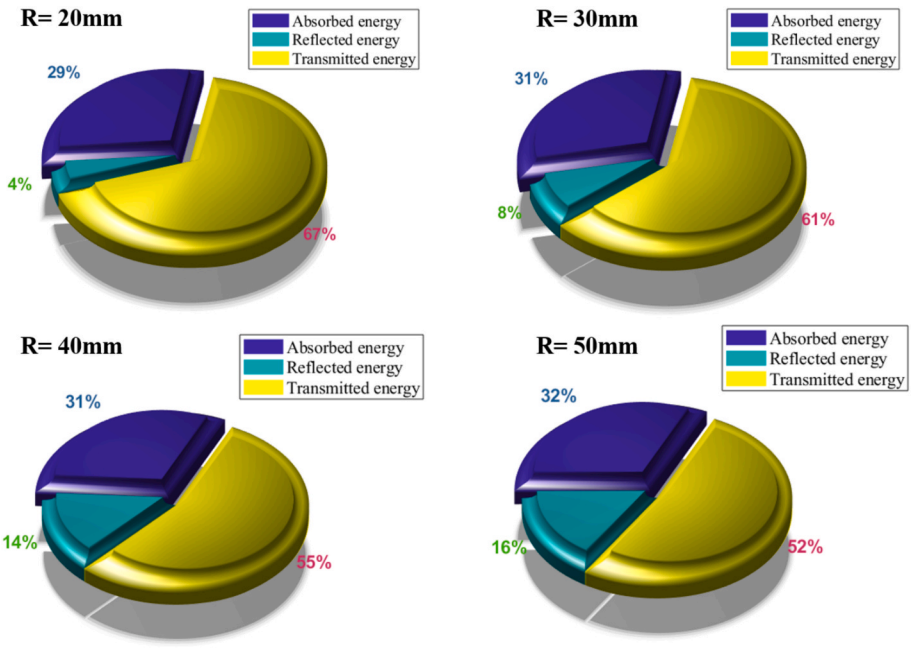

Fig. 16. Sound energy distribution for SBHs with varying radii.

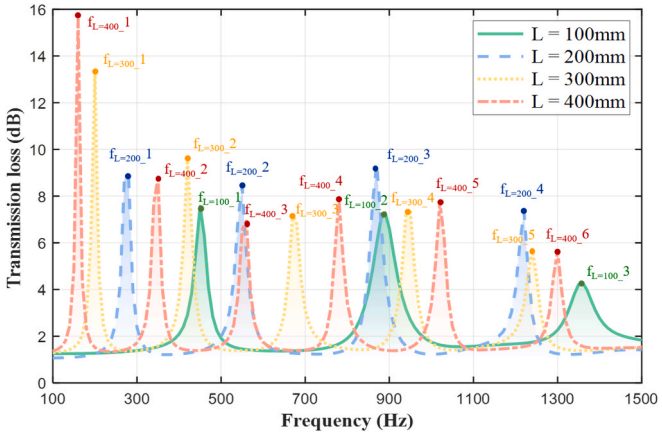

Fig. 17. Comparison of TL curves for SBHs with different lengths.

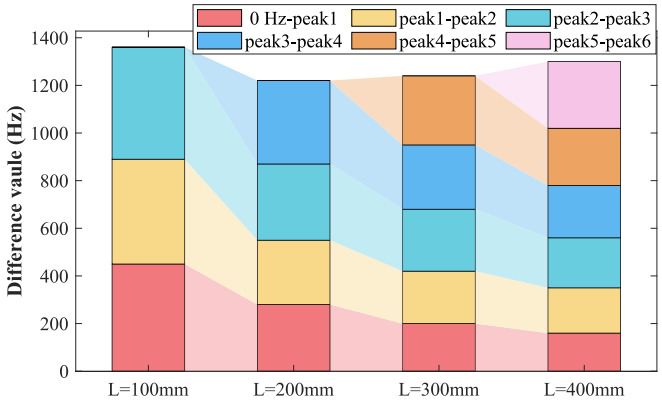

Fig. 18. Frequency intervals between neighboring TL peaks for SBHs with varying lengths.

Table 3
Overall mean phase velocity at 1000 Hz for SBHs of varying lengths.

	L = 100 mm	*L = 200 mm*	*L = 300 mm*	*L = 400 mm*
$\overline{c_h}$(m/s)	133.3	144.5	158.7	168.0

with an inner radius of 30 mm, an outer radius of 36 mm, and a length of 200 mm was machined and bisected. Several grooves of 2 mm width and 0.5 mm depth were created on the inner wall of the cylinder to accommodate mounting rings. The rings, with an outer radius of 30.5 mm, were fabricated with inner radius of 27 mm, 24 mm, 21 mm, 18 mm, 15 mm, 12 mm, 9 mm, 6 mm and 3 mm. One end of the cylinder featured internal threading, 5 mm in length, to facilitate attachment to a pipe. The first ring was positioned 15 mm from the threads, the last ring was 18 mm from the end of the SBH, and the remaining rings were evenly spaced 18 mm apart. The experiments also included a cavity structure with the same inner radius and length as the SBH, created by removing all rings. Both the SBH and the cavity structure were connected to the main duct via a small connector.

The Perfectly Matched Layer (PML) is utilized in finite element calculations to prevent reflections at the end of the duct. However, achieving complete sound absorption at the duct termination is challenging in practice. Consequently, the two-load method [49] was adopted to measure the TL of SBH. The experimental setup, illustrated in Fig. 20, comprises a square duct made of acrylic with a wall thickness of 19 mm and the cross section of 100 x 100 mm, a test sample, four 1/4-inch microphones (BSWA, MPA416), a loudspeaker, a signal generator, and a four-channel data acquisition board (National Instruments, model USB-4431). The sample is flushed-mounted on the duct wall. A loudspeaker connected with the signal generator was fixed at one end of the duct to generate white noise as acoustic excitation. Two microphones were flush-mounted upstream the SBH, and two others downstream. The separation distance between the microphones is 100 mm, and the spacing between the sample and the nearest microphone was 330 mm, both upstream and downstream. Two distinct end loads, as shown in Fig. 21, were employed: a rigid baffle and a duct stuffed with sound absorption material.

Fig. 19. SBH sample: (a) exterior view; (b) sectional view; (c) interior view.

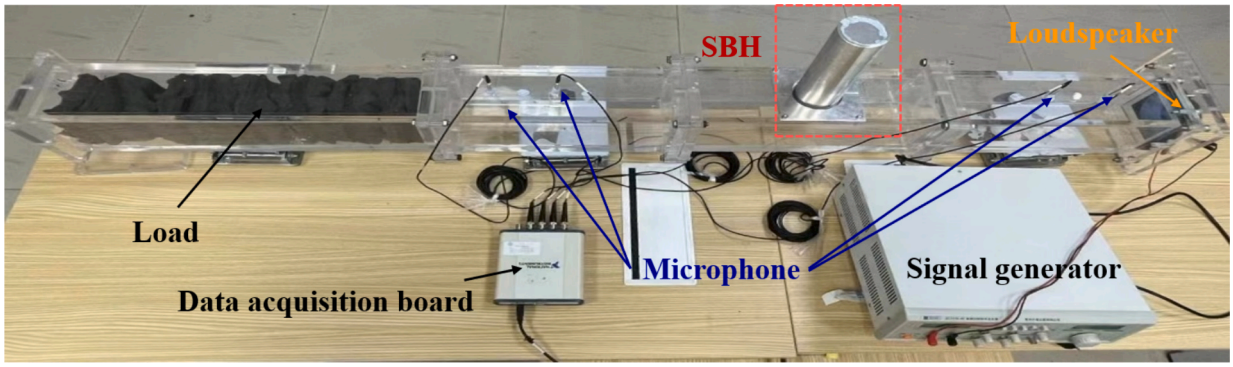

Fig. 20. Experimental setup.

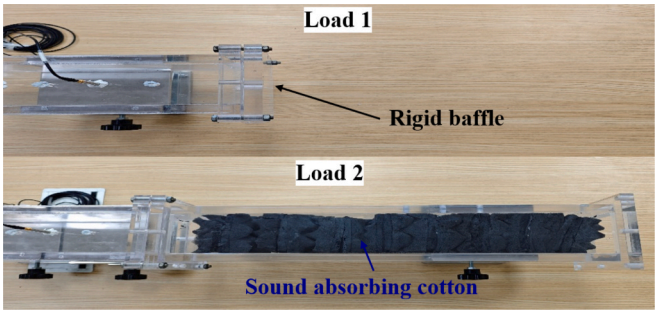

Fig. 21. Two different duct end loads.

5.2. Validations

The measured and simulated TL curves for the cavity and SBH structure are presented and compared in Fig. 22. The experimental results indicated that the SBH achieved five muffling peaks between 200 and 1600 Hz, with TL peak values ranging from 5-8 dB, and a broadband muffling characteristic of approximately 1.9 dB across the analyzed frequency range. Conversely, the cavity showed pronounced muffling peaks only at 370 Hz and 1080 Hz, with negligible muffling effects outside these peak frequencies, showing rather narrowband muffling performance. The comparisons show that the simulation results can well capture the TL peak magnitudes and locations. Observed discrepancies can mainly be attributed to the inevitable imperfections in the manufactured sample and imperfect fitting of the structure to the impedance tube. Nevertheless, the discrepancies between the experimental and calculated results are deemed within an acceptable range, thus validating the muffling ability of the SBHs.

6. Conclusions

The muffling characteristics and mechanisms of a Sonic Black Hole are investigated both numerically and experimentally. The investigated SBH structure exhibits five distinct muffling peaks within the 100–1600 Hz range, with a maximum attenuation of 9.4 dB. Additionally, the structure maintains a consistent attenuation of approximately 1.6 dB across a broad frequency range, highlighting its wideband, multi-peak muffling characteristics. The thermo-viscous dissipation within the SBH contributes to its sound absorption capacity, ensuring effective broadband noise attenuation. It was found that when the sound pressure distribution inside the SBH corresponds to $i/4$ wavelength (where i is odd) pattern, both the absorption and reflection effects of the structure are maximized, resulting in the occurrence of muffling peaks. The slow wave effect within the SBH decreases the muffling peak frequency, leading to the emergence of multiple muffling peaks within the analyzed frequency band. Consequently, the structure exhibits muffling characteristics with multiple peaks and a broad bandwidth. Structural parameter studies reveal that increasing the number of internal rings reduce the internal phase velocity of sound wave, resulting in downshifting and a greater number of muffling peaks within a specific frequency range. Increasing the radius of the muffler significantly enhances sound wave reflection, thereby enhancing the overall muffling effect. While the length of the SBH has minimal impact on the overall muffling effect, longer structures tend to lower the peak frequency, reduce the

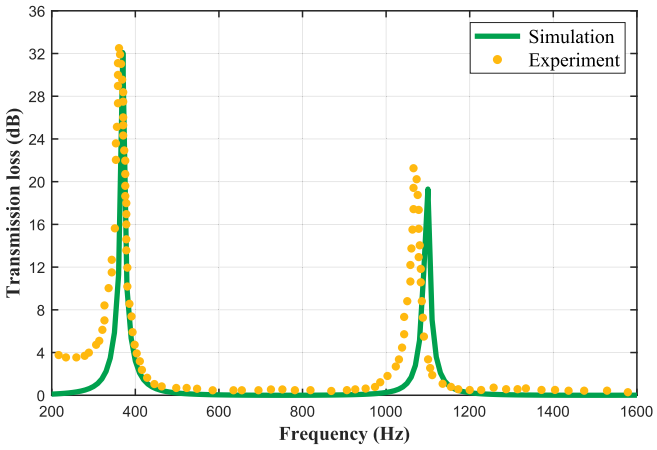

(a)

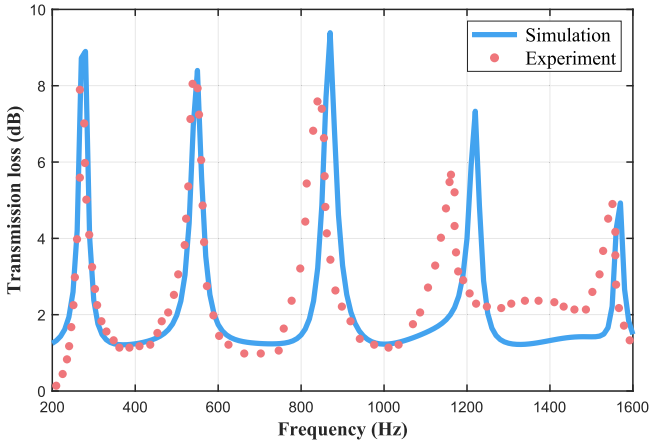

(b)

Fig. 22. Comparison between experimental and calculated results for (a) cavity and (b) SBH.

frequency intervals between muffling peaks and yield more peaks within the targeted frequency band.

CRediT authorship contribution statement

Xiaoqi Zhang: Writing – review & editing, Writing – original draft, Validation, Methodology, Formal analysis. **Lilong Wang:** Writing – review & editing, Writing – original draft, Validation, Methodology, Formal analysis. **Li Cheng:** Supervision. **Heow Pueh Lee:** Supervision. **Linke Zhang:** Writing – review & editing, Supervision, Resources.

Declaration of competing interest

The authors declare that they have no known competing financial interests or personal relationships that could have appeared to influence the work reported in this paper.

Acknowledgements

The research reported here was supported by Wuhan Talent Program for Outstanding Young Scholars (202402jc0069) and China Scholarship Council (202306950060).

Data availability

Data will be made available on request.

References

[1] Wu L, Liang W, Sha D. A novel adaptive noise reduction method for field natural gas pipeline defect detection signals. Int J Press Vessel Pip 2022;199:104761.
[2] Khaiwal R, Singh T, Tripathy J, Mor S, Munja S, Patro B, et al. Assessment of noise pollution in and around a sensitive zone in North India and its non-auditory impacts. Sci Total Environ 2016;566:981–7.
[3] Xu C, Zhang Y, Cheng B, Li L, Zhang M. Study on environmental Kuznets Curve for noise pollution: a case of 111 Chinese cities. Sustain Cities Soc 2020;63:102493.
[4] Li W, Yi G, Chen Z, Wu J, Wang D. Association of occupational noise exposure, bilateral hearing loss with hypertension among Chinese workers. J Hypertens 2021;39:643–50.
[5] Li S, Daniel Y, Janet Y, Bradley M, Esther Y, Huang L, et al. Noise sensitivity associated with nonrestorative sleep in Chinese adults: a cross-sectional study. BMC Public Health 2021;21:643.
[6] Yi S, Lee B. Three-dimensional acoustic analysis of circular expansion chambers with a side inlet and a side outlet. Journal of the Acoustical society of American 1986;79:1299–306.
[7] Selamet A, Xu M, Lee I, Huff N. Analytical approach for sound attenuation in perforated dissipative silencers with inlet/outlet extensions. J Acoust Soc Am 2005; 117:2078–89.
[8] Kulkarni M, Ingle R. Effect of Extended Inlet and Outlet Lengths on Transmission loss of double expansion Chamber Reactive Muffler. International Journal of Vehicle Structures and Systems 2022;14:135–7.
[9] Xu MB, Selamet A, Lee IJ, Huff NT. Sound attenuation in dissipative expansion chambers. J Sound Vib 2004;272:1125.
[10] Denia FD, Sánchez-Orgaz E, Baeza L, Kirby R. Point collocation scheme in silencers with temperature gradient and mean flow. J Comput Appl Math 2016;291:127–41.
[11] Chen Z, Ji Z, Huang H. Acoustic impedance of perforated plates in the presence of bias flow. J Sound Vib 2019;446:159–75.
[12] Mironov MA. Propagation of a flexural wave in a plate whose thickness decreases smoothly to zero in a finite interval. Soviet Physics - Acoustics 1988;34:318–9.
[13] Krylov VV, Tilman F. Acoustic black holes for flexural waves as effective vibration dampers. J Sound Vib 2004;274:605–19.
[14] Deng J, Gao N, Chen X, Han B, Ji H. Evanescent waves in a metabeam attached with lossy acoustic black hole pillars. Mech Syst Sig Process 2023;191:110182.
[15] Mccormick CA, Shepherd MR. Design optimization and performance comparison of three styles of one-dimensional acoustic black hole vibration absorbers. J Sound Vib 2020;470:115164.
[16] Deng J, Guasch O, Maxit L, Zheng L. Transmission loss of plates with multiple embedded acoustic black holes using statistical modal energy distribution analysis. Mech Syst Sig Process 2021;150:107262.
[17] Zhou T, Cheng L. Planar Swirl-shaped Acoustic Black Hole Absorbers for Multi-directional Vibration suppression. J Sound Vib 2022;516:116500.
[18] Deng J, Guasch O, Maxit L, Zheng L. Annular acoustic black holes to reduce sound radiation from cylindrical shells. Mech Syst Sig Process 2021;158:107722.
[19] Mironov MA, Pislyakov VV. One-dimensional acoustic waves in retarding structures with propagation velocity tending to zero(Article). Acoust Phys 2002;48: 347–52.
[20] Mi Y, Zhai W, Cheng L, Xi C, Yu X. Wave trapping by acoustic black hole: Simultaneous reduction of sound reflection and transmission. Appl Phys Lett 2021; 118:1–5.
[21] Mousavi A, Berggren M, Wadbro E. How the waveguide acoustic black hole works: a study of possible damping mechanisms. J Acoust Soc Am 2022;151:4279.
[22] Su L, Chen J, He X, Wang Y, Liang X, Chu J, et al. The acoustic streaming effects of sonic black hole. Mod Phys Lett B 2022;36:2250079.
[23] Deng J, Guasch O. Sound waves in continuum models of periodic sonic black holes. Mech Syst Sig Process 2023;205:110853.
[24] Guasch O, Sanchez-Martín P, Ghilardi D. Application of the transfer matrix approximation for wave propagation in a metafluid representing an acoustic black hole duct termination. App Math Model 2020;77:1881–93.
[25] Hollkamp JP, Semperlotti F. Application of fractional order operators to the simulation of ducts with acoustic black hole terminations. J Sound Vib 2020;465: 115035.
[26] Ou Y, Zhao Y. Design, analysis, and experimental validation of a sonic black hole structure for near-perfect broadband sound absorption. Appl Acoust 2024;225: 110196.
[27] Ei-Ouahabi A, Krylov V V, O'boy D. Investigation of the acoustic black hole termination for sound waves propagating in cylindrical waveguides; proceedings of the 44th International Congress and Exposition on Noise Control Engineering, F, 2015 [C].
[28] Ei-Ouahabi A, Krylove V V, O'boy D. Experimental investigation of the acoustic black hole for sound absorption in air; proceedings of the Proceedings of 22nd International Congress on Sound and Vibration, Florence, Italy, 2015, F, 2015 [C].
[29] Mironov MA, Pislyakov VV. One-dimensional sonic black holes: exact analytical solution and experiments. J Sound Vib 2020;473:115223.
[30] Chen Y, Yu K, Fu Q, Zhang J, Lu X. Modification of the transfer matrix method for the sonic black hole and broadening effective absorption band. Mech Syst Sig Process 2024;220:111660.

[31] Guasch O, Arnela M, SáNchez-MartíN P. Transfer matrices to characterize linear and quadratic acoustic black holes in duct terminations [J]. Journal of Sound and Vibration, 2017, 395: 65-79.
[32] Červenka M, Bednařík M. On the role of resonance and thermoviscous losses in an implementation of "acoustic black hole" for sound absorption in air. Wave Motion 2022;114:103039.
[33] Zhang X, He N, Cheng L, Yu X, Zhang L, Hu F. Sound absorption in sonic black holes: Wave retarding effect with broadband cavity resonance. Appl Acoust 2024; 221:110007.
[34] Li Y, Li L, Xiao L, Cheng L, Yu X. Enhancing ventilation window acoustics with sonic black hole integration: a performance evaluation. Appl Acoust 2025;229: 110388.
[35] Peng L, Mao Q, Wang H, Lai L, Shi Q, Chen M. Enhanced sound absorption with the combined sonic black holes. Appl Acoust 2024;219:109932.
[36] Zhang X, Cheng L. Broadband and low frequency sound absorption by Sonic black holes with Micro-perforated boundaries. J Sound Vib 2021;512:116401.
[37] Li S, Xia J, Yu X, Zhang X, Cheng L. A Sonic Black Hole Structure with Perforated Boundary for Slow Wave Generation. J Sound Vib 2023;559:117781.
[38] Mi Y, Cheng L, Zhai W, Yu X. Broadband low-frequency sound attenuation in duct with embedded periodic sonic black holes. J Sound Vib 2022;536:117138.
[39] Bravo T, Maury C. Broadband sound attenuation and absorption by duct silencers based on the acoustic black hole effect: simulations and experiments. J Sound Vib 2023;561:117825.
[40] Lee S, Jang J, Song K. Enhanced acoustic attenuation in a coiled meta-silencer: Broadband low-frequency noise control through rainbow trapping. Mech Syst Sig Process 2025;222:111744.
[41] Li S, Yu X, Cheng L. Enhancing wave retarding and sound absorption performances in perforation-modulated sonic black hole structures. J Sound Vib 2025;596: 118765.
[42] Tang Y, Ren S, Meng H, Xin F, Huang L, Chen T, et al. Hybrid acoustic metamaterial as super absorber for broadband low-frequency sound. Sci Rep 2017; 7:43340.
[43] Duan M, Yu C, Xu Z, Xin F, Lu T. Acoustic impedance regulation of Helmholtz resonators for perfect sound absorption via roughened embedded necks. Appl Phys Lett 2020;117:151904.
[44] Duan M, Yu C, Xin F, Lu T. Tunable underwater acoustic metamaterials via quasi-Helmholtz resonance: from low-frequency to ultra-broadband. Appl Phys Lett 2021;118:071904.
[45] Multiphysics C. Acoustics Module User's Guide. 2022.
[46] Carl QH, Richard AC. Noise reduction using a quarter wave tube with different orifice geometries. Appl Acoust 2014;76:180–6.
[47] Umnova O, Brooke D, Leclaire P, Dupont T. Multiple resonances in lossy acoustic black holes - theory and experiment. J Sound Vib 2022;543:117377.
[48] Woo H. Basic physics of elastography; proceedings of the 45th Annual Congress of Korean Society of Ultrasound in Medicine, F, 2014 [C].
[49] Tao Z, Seybert AF. A review of current techniques for measuring muffler transmission loss. SAE Trans 2003;112:2096–100.